Engineering Applications of Artificial Intelligence 150 (2025) 110636

Contents lists available at ScienceDirect

Engineering Applications of Artificial Intelligence

journal homepage: www.elsevier.com/locate/engappai

Two-dimensional temperature field prediction with in-situ data in metal additive manufacturing using physics-informed neural networks

Pouyan Sajadi, Mostafa Rahmani Dehaghani, Yifan Tang, G. Gary Wang *

Product Design and Optimization Laboratory, Simon Fraser University, Surrey, BC, Canada

ARTICLE INFO

Keywords:
Metal additive manufacturing
Physics-informed neural networks
Temperature field prediction
Data-driven modeling
Physics-informed loss function

ABSTRACT

Accurately predicting the temperature field in metal additive manufacturing (AM) processes is critical for preventing overheating, adjusting process parameters, and ensuring process stability. While physics-based computational models offer precision, they are often time-consuming and unsuitable for real-time predictions. Machine learning models, on the other hand, rely heavily on high-quality datasets, which can be costly and difficult to obtain in the metal AM domain. Existing studies on physics-informed neural networks (PINNs) have made progress in integrating physics with machine learning but often lack in-situ data integration, which is essential for capturing real-time thermal dynamics. Additionally, their methodologies are typically heavily dependent on specific process characteristics, limiting their flexibility. Our work addresses these gaps by introducing a PINN-based framework specifically designed for temperature field prediction in metal AM. The framework incorporates in-situ temperature data gathered during the manufacturing process, combining it with physics-informed inputs and a custom loss function. The approach is demonstrated through two case studies. In the first case, using a small set of experimental data, the model achieves an error below 3 % with a mean absolute error (MAE) of 11 °C. In the second case, using simulation data, the model achieves an error below 1 % with an MAE of 7 °C. In addition, the framework shows promising adaptability for different metal AM scenarios with different geometries, deposition patterns, and process parameters.

1. Introduction

Metal additive manufacturing (AM) has emerged as a transformative technology, finding applications across a spectrum of industries, including aerospace, defense, and biomedicine. Its attractiveness stems from its capacity to create custom-designed 3D objects layer-by-layer, enabling mass customization, lightweight designs, efficient material recyclability, and shortened lead times (Shamsaei et al., 2015). Metal AM comprises a variety of technologies, each offering a unique method for fabricating metal parts layer by layer. These technologies include directed energy deposition (DED), vat polymerization, material extrusion, binder jetting, material jetting, powder bed fusion, and sheet lamination, as illustrated in.

Fig. 1. Each technology differs in how materials are deposited and fused, providing specific advantages based on the application. Among these, DED stands out for its ability to simultaneously deposit and fuse material using an energy source, such as a laser or plasma arc. In DED, metal in powder or wire form is fed into a melt pool created by the energy source, where it fuses to the underlying material. As the energy source moves, new layers are deposited and solidified. This process is particularly well-suited for creating large-scale parts, repairing components, or adding material to existing structures (Busachi et al., 2017).

In the metal AM process, including DED, rapid heating and cooling cycles typically occur, inducing substantial fluctuations in the temperature field within both the substrate and deposited layers (Thompson et al., 2015). This dynamic thermal environment is a critical determinant of the final product's quality, leading to variations in microstructure (Bontha et al., 2006; Lippold et al., 2011), porosity (Barua et al., 2014), as well as residual stress and strain states (Shamsaei et al., 2015; H. Yan et al., 2018). Consequently, a precise understanding and comprehensive analysis of thermal conditions are imperative for effectively controlling the AM deposition process (Z. Yan et al., 2018).

In this dynamic context, the integration of digital twins (DT) assumes a pivotal role, serving as a bridge between the physical and digital realms. A digital twin represents a virtual replica of the physical AM system (Yao et al., 2023), functioning in real-time synchronization with the actual manufacturing process. Within this framework, real-time or near-real-time prediction of temperature fields emerges not only as a

* Corresponding author.
E-mail addresses: sps11@sfu.ca (P. Sajadi), mra91@sfu.ca (M.R. Dehaghani), yta88@sfu.ca (Y. Tang), gary_wang@sfu.ca (G.G. Wang).

https://doi.org/10.1016/j.engappai.2025.110636
Received 16 January 2024; Received in revised form 10 March 2025; Accepted 17 March 2025
Available online 23 March 2025

pivotal element but also as a pathway towards optimizing parameters (Hosseini et al., 2023), minimizing defects (Khairallah et al., 2016; Ren et al., 2019), ensuring consistent product quality (Zheng et al., 2008), reducing waste, enabling predictive maintenance, and continually enhancing the efficiency and reliability of metal AM technology (Zhang et al., 2020).

Physics-based computational models, such as the finite element method (FEM) and computational fluid dynamics (CFD), are extensively studied for predicting thermal behavior in AM, most of which are inherently multiscale and multiphysical (Razavykia et al., 2020). These models use partial differential equations (PDEs) like Navier–Stokes and heat transfer equations to understand thermal history and temperature distribution. FEM models, preferred by (Roberts et al., 2009), offer computational efficiency over CFD, particularly for analyzing solid heat transfer (Denlinger and Michaleris, 2016; Liao et al., 2022a).

In their study, Li et al. (2020) employed a thermal-fluid model that integrated the level set method and Lagrangian particle tracking for laser powder-bed fusion (LPBF), which provided a detailed representation of melt pool dynamics. While this model delivered a high level of detail, it was computationally expensive similar to other FEM-based approaches, and was less suited for real-time applications. Similarly, J. Yan et al. (2018) developed a thermal flow model to simulate melt pool dynamics in laser spot melting, offering important insights into flow behavior but requiring highly accurate input parameters, which are difficult to determine experimentally. Bai et al. (2013) attempted to address this issue by using infrared (IR) temperature data to calibrate uncertain input parameters, thus improving the accuracy of their thermal simulations. While this approach helps to reduce the uncertainty in input parameters, it requires real-time experimental data and frequent recalibration, making it less suited for dynamic, real-time applications. Most of these physics-based studies (e.g., Heigel et al., 2015; Darabi et al., 2022) focus primarily on examining the effects of varying process parameters—such as laser power, scanning speed, and material properties—on thermal behavior, rather than being designed for real-time predictive applications. Darabi et al. (2022), for example, used a phase-field model combined with finite element analysis to explore the thermal effects in the DED process of Inconel 625, analyzing how changes in laser power influenced melt pool dimensions and solidification rates.

Despite advancements in numerical models for simulating temperature distributions in metal AM processes, there exist several limitations that hinder the practical use in real-world applications, including real-time prediction, the necessity for deep physical and mathematical understanding, and the need for high-performance hardware (X. Ren et al., 2020).

As an alternative to physics-based numerical models, data-driven methods are employed in modeling the intricate behaviors of AM processes. The study of data-driven thermal prediction can be classified into two main categories based on their input variables. The first category comprises models that solely map process parameters and the properties of parts to temperature profiles (Mozaffar et al., 2018; Roy and Wodo, 2020). In contrast, the second category includes models that incorporate temperature data from adjacent elements or previous time steps during the AM process, accounting for thermal transfer effects (Paul et al., 2019; K. Ren et al., 2020; Stathatos and Vosniakos, 2019; Tang et al., 2023). In the first category of studies, Roy and Wodo (2020) and Mozaffar et al. (2018) used FEM calibration and recurrent neural network (RNN)-based models to predict the local thermal history with errors below 5 % and a normalized mean squared error (MSE) of 2.97×10^{-5}, respectively. While both models can effectively forecast temperature fields inside fabricated parts and on their surfaces, they have limitations. Mozaffar et al.'s model requires a large dataset (250,000 points), which is time-consuming to generate, and it relies on specific geometric features, limiting its generalizability to more complex shapes. Roy and Wodo's model, though using a smaller dataset (26,000 points), still involves a considerable amount of data. In the second category, studies (Paul et al., 2019; K. Ren et al., 2020; Stathatos and Vosniakos, 2019) utilized artificial neural networks and iterative prediction methods, incorporating factors such as past temperatures, surrounding elements, and element locations relative to laser inputs. These models achieved improved accuracy for future time steps and various laser paths. However, Paul's model required 54,450 data points, while Ren's model needed 9 million data points to achieve relative errors below 1 %. Additionally, these models rely heavily on point-wise simulation data, and their applicability with experimental data has not been demonstrated, limiting their real-world validation. Additionally, Tang et al. (2023) utilized temperatures from specific points on the printed layer to predict the complete temperature field for the yet-to-print layer. An artificial neural network predicts temperature profiles for these specific points, followed by the use of a reduced order model to reconstruct the temperature profile for the entire layer. They achieved a relative error of profile (REOP) as low as 0.02 on simulation data. However, the study's focus on thin wall structures limits its applicability to more complex geometries in metal AM.

Data-driven models offer computational efficiency and reduced dependence on comprehensive physical knowledge. However, they exhibit certain drawbacks. They often operate as "black box" systems, lacking transparency in their decision-making processes. They require substantial amounts of data for effective training, which can be time-consuming and expensive, especially in the context of metal AM, where obtaining extensive and high-quality training data is costly or challenging.

Physics-Informed Neural Networks (PINNs) represent an innovative ML paradigm that integrates the laws of physics, typically described by PDEs, directly into the neural network architecture (Raissi et al., 2019). PINNs have gained significant traction in recent years across various scientific domains, such as fluid mechanics (Jin et al., 2021), electromagnetic analysis (Noakoasteen et al., 2020), and crack recognition (Shukla et al., 2020), where they leverage physical principles to enhance predictive accuracy even when confronted with limited data. In the realm of metal AM, PINNs can accurately predict temperature fields and melt pool dimensions while optimizing computational efficiency

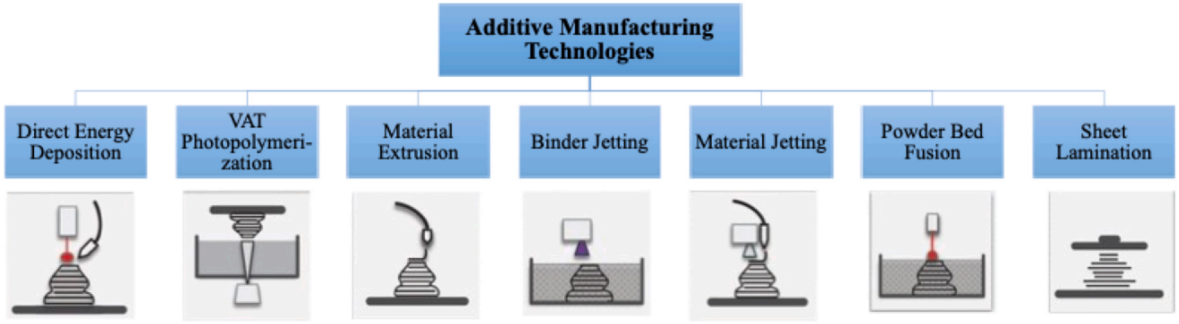

Fig. 1. Additive manufacturing technologies.

(Hosseini et al., 2023; Li et al., 2023). As a pioneering work, Zhu et al. (2021) employed a PINN to predict temperature and melt pool fluid dynamics in LPBF by incorporating essential conservation equations and utilizing the finite element simulation data. These simulations run up to 2.0 milli-seconds but only a limited portion from 1.2 to 1.5 milli-seconds is used as labeled training data. In another study focused on the melt pool, Jiang et al. (2023) used the heat transfer equation alongside a small amount of data obtained from simulations to predict the temperature field and melt pool dimensions. Xie et al. (2022a) integrated heat transfer laws into their PINN framework to predict temperature fields in single-layer and multi-layer DED processes. Their model surpasses data-driven methods in both scenarios, achieving an accuracy of over 90 % with just 4000 training data points, in contrast to tens of thousands training points employed by most data-driven models. Similarly, heat transfer principles and partially observed temperature data from infrared cameras were employed to accurately predict the temperature history and identify hidden parameters, such as the laser absorptivity, C_P, and the material thermal conductivity, within the process (Liao et al., 2022b). This research also emphasizes the advantageous role of transfer learning techniques in enhancing training efficiency and boosting prediction accuracy.

The detailed information of studies on PINNs to predict temperature fields is summarized in Table 1. While significant progress has been made in integrating physics knowledge with ML models, these advancements are often constrained to modeling only a short duration of the process, typically less than a second. Furthermore, a key limitation is the lack of in-situ data integration in their modeling approaches, a crucial element that enables real-time applications and provides valuable insight into the actual metal AM process. Lastly, current modeling schemes tend to be tailored to single tracks and constant geometries, falling short when applied to processes with varying geometries and deposition patterns.

To address these existing gaps, this paper introduces a novel physics-informed Convolutional Long Short-Term Memory (PI-ConvLSTM) framework. This framework leverages in-situ temperature field data collected during the manufacturing process to predict the 2-D temperature field of the part for future timestamps. The proposed framework shows promising accuracy and versatility for scenarios involving different geometries, deposition patterns, and process parameters without requiring specific adjustments for each case.

The rest of the paper is organized as follows: Section 2 introduces the basics of PINNs and the governing equations employed for modeling. This Section further delves into each component of the proposed PI-ConvLSTM framework. In Section 3, the paper details two distinct applications used to validate the framework with discussions of the results for each application. Section 4 is dedicated to presenting insights, outlining limitations, and exploring prospects. Finally, Section 5 encapsulates the paper with a conclusion and suggests potential avenues for future work.

2. Methods

2.1. General PINN model

Conventional neural networks primarily operate by mapping input data to desired outputs through training and rely heavily on the quantity and quality of labeled data for effective learning. Meanwhile, in practical scenarios, physical systems are often governed by underlying physical laws represented by PDEs.

PINNs seamlessly integrate the PDEs and information from measurements into the neural network's loss function through automatic differentiation. In its general form, PDEs can be expressed as:

$$u_t(x,t) + N(u:\lambda) = 0, x \in \Omega, t \in [0,T] \tag{1}$$

where $u_t(x,t)$ serves a dual purpose, acting as both the actual PDE solution and the target neural network's output. The term $N(u:\lambda)$ embodies a nonlinear differential operator, with λ encapsulating relevant parameters within the PDEs. The spatial domain is denoted by Ω, while $[0,T]$ represents the temporal extent. The core of PINNs lies the concept of residual as a quantifiable measure of PDE compliance. Mathematically, the residual of a PDE is expressed as:

$$Res = \widehat{u}(x,t) + N(u:\lambda) \tag{2}$$

This residual encapsulates the underlying physical law represented by the PDEs. As the predicted output $\widehat{u}(x,t)$ of the neural network approaches the actual solution $u_t(x,t)$, the residual progressively diminishes. Therefore, by incorporating this residual into the model's loss function, it serves as a regularization factor, effectively constraining the neural network to adhere more closely to the governing physical principles encoded by the PDEs. Additionally, PINNs incorporate boundary and initial conditions, represented by Equations (3) and (4), to establish a well-posed system.

$$u_t(x,t) - B(x,t) = 0, x \in \partial\Omega \tag{3}$$

$$u_t(x,0) - I(x) = 0, x \in \Omega \tag{4}$$

Here, $B(x,t)$ represents boundary conditions, and $I(x)$ signifies initial conditions. Integrating these physical laws into the loss function is essential for enforcing system constraints. These physical laws, alongside the supervised loss of data measurements (Equations (5)–(8)), become integral components of the neural network's loss function,

Table 1
A summary of PINN studies for temperature field prediction of metal AM processes (MAPE is mean absolute percentage error, MRE is mean relative error and RMSE is root mean square error).

Study	Process	Physics incorporated	Inputs	Predicted output	Number of data points	Accuracy
Hosseini et al. (2023)	Single-track LPBF	Thermal energy conservation equation	x, y, z, t, process parameters, material properties	Temperature field	NA	MAPE = 4.5 %
Shukla et al. (2020)	Single-track laser metal deposition	Heat transfer in deposition and cooling stage	x, y, z, t	Temperature field	NA	MRE = 0.81 % for three sample points
Li et al. (2023)	Single-track selective laser beam melting	conservation laws of momentum, mass (Navier-Stokes), and energy	x, y, z, t	Melt pool temperature and dynamics	10,000,000 simulation data	MRE = 5.9 % for melt pool length
Zhu et al. (2021)	Single-track DED	Heat transfer	x, y, z, t	melt pool size and temperature distribution	NA	MRE = 2 %
Jiang et al. (2023)	Single-track DED	Heat transfer	x, y, z, t	Temperature field	30,000 simulation data	MRE = 2.05 % for average of three multi-layer cases
Xie et al., 2022	Single-track DED	Heat transfer	x, y, z, t	Temperature field	100,000 simulation data	RMSE (K) with clean data = 3.59

resulting in Equation (9):

$$L_{pde} = \frac{1}{N_p}\sum_{i=1}^{N_p} Res_{pde}^2 \tag{5}$$

$$L_{ic} = \frac{1}{N_i}\sum_{i=1}^{N_i} (\hat{u}_i - I_i(x))^2 \tag{6}$$

$$L_{bc} = \frac{1}{N_b}\sum_{i=1}^{N_b} (\hat{u}_i - B_i(x,t))^2 \tag{7}$$

$$L_{data} = \frac{1}{N_d}\sum_{i=1}^{N_d} (\hat{u}_i - u_i)^2 \tag{8}$$

$$L_{total} = w_p L_{pde} + w_i L_{ic} + w_b L_{bc} + w_d L_{data} \tag{9}$$

Here, L represents the loss function associated with each of the components in the provided equations; Res_{pde} is the residual of the PDE and $\hat{u}_i$ is the neural network's output and u_i represents the ground truth data points from the supervised learning dataset. In Equation (9), components are weighted using w_p, w_i, w_b, and w_d, respectively, and involve N_p, N_i, N_b, and N_d sampling points associated with each respective loss term. The network is effectively trained by minimizing the loss, employing gradient-based optimizers like Adam (Kingma and Ba, 2014) and L-BFGS (Byrd et al., 1995), all facilitated through the process of backpropagation. An overview of the PINN algorithm is depicted in Fig. 2.

2.2. Governing equations

In this Section, we introduce the governing equations for thermal prediction in this paper. Our focus is on modeling heat conduction in the metal AM process. With an exclusion of factors such as fluid flow and vaporization heat loss, the transient heat transfer during the process is represented by the following heat conduction PDE (Holman, 1986):

$$\rho C_p \frac{\partial(T(x,y,t))}{\partial t} = \frac{\partial}{\partial x}\left(k\frac{\partial T(x,y,t)}{\partial x}\right) + \frac{\partial}{\partial y}\left(k\frac{\partial T(x,y,t)}{\partial y}\right), x,y \in \Omega, t \in [0, t_{end}] \tag{10}$$

where $T(x,y,t)$ is the corresponding temperature of position (x,y) at time t, ρ is the density of the part material, C_p is the specific heat, and k is the thermal conductivity. The initial condition is set equal to the ambient air temperature, T_{amb}. The boundary conditions are applied to all surfaces, except for the top surface where the laser heat flux is applied, accounting for the heat radiation and convection with the surrounding air.

For surfaces other than the top surface:

$$-k\frac{\partial T}{\partial \vec{n}} = h(T - T_{amb}) + \sigma\varepsilon\left(T^4 - {T_{amb}}^4\right), x \in \partial\Omega \tag{11}$$

For the top surface, with an additional term corresponding to the laser heat flux:

$$-k\frac{\partial T}{\partial \vec{n}} = h_c(T - T_{amb}) + \sigma\varepsilon\left(T^4 - {T_{amb}}^4\right) + Q_{laser}, x \in \partial\Omega_{top} \tag{12}$$

Here, $\frac{\partial T}{\partial \vec{n}}$ denotes the normal derivative perpendicular to the boundary. The coefficient h signifies the heat convection coefficient characterizing the interaction between the substrate and air, while σ stands for the Stefan–Boltzmann constant, and ε represents the heat radiation coefficient. Q_{laser} denotes the energy produced by the laser heat source per unit volume. These boundary conditions are essential for modeling the heat transfer and energy flow in the system.

2.3. Proposed online PI-ConvLSTM framework

In this section, we will explore the physics-informed ConvLSTM framework designed to address the challenging task of predicting the temperature field during the metal AM process. This framework leverages two types of inputs: sequential thermal images and a physics-informed (PI) input matrix derived from process parameters. More specifically, the first input is a sequence of w thermal images from timestamps $(t - w)$ to t, providing temporal information about the evolving temperature field. The second input is a PI input matrix, constructed from process parameters such as laser power, absorptivity, and beam radius. This input is a 2D matrix representing the spatial distribution of laser heat flux, incorporating process parameters in a physically meaningful way to provide additional context for the model.

Using these two inputs, the model predicts the temperature field at timestamp $(t + i)$, capturing the thermal distribution at a future point in time. Here, w represents the window size for the input, and i denotes the timestamp in the future for which we aim to predict the temperature field. It's essential to note that both w and i are hyperparameters, and their significance will be elaborated on in the following sections.

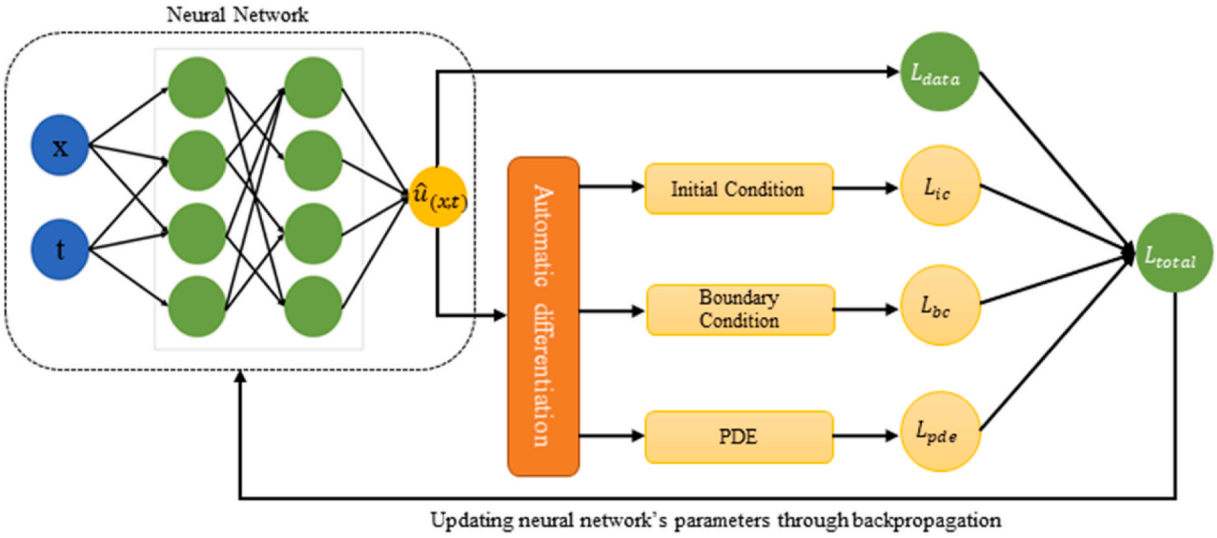

Fig. 2. During training, the neural network predicts the output $\hat{u}(x,t)$, and computes the physics loss function, evaluating the system's adherence to physical laws. This loss function encompasses various components, including data-driven and physics losses, which are then minimized through backpropagation.

This problem is inherently high-dimensional, given that the inputs and outputs consist of 2D thermal images. Furthermore, considering the temporal relationship between inputs and outputs due to the sequential nature of the data, we can view this problem as a 2D sequential modeling challenge. In Fig. 3, we provide an illustrative overview of our comprehensive framework, comprised of three key components: the neural network, Physics-informed (PI) loss, and Physics-informed (PI) input. These elements together underpin our strategy for addressing the complex challenge of predicting temperature distributions in a system with spatial and temporal dependencies. In the following sections, we will delve into each of these components, offering a closer look at their specific functions and how they work together within the framework.

2.3.1. Model architecture

To tackle such complex and high-dimensional tasks, the choice of neural network architecture is crucial. In the literature, Convolutional Neural networks (CNN) are recognized for their ability to manage high-dimensional data by efficiently sharing parameters across layers. Spatial dependencies within 2D-to-2D modeling tasks are effectively captured by CNNs (Neupane et al., 2021; Wu et al., 2023; Zhou et al., 2021), which employ convolutional layers to hierarchically extract features from the input data, enabling the learning of complex patterns.

Complementarily, the long short-term memory (LSTM) architecture excels at capturing temporal dependencies within sequential data (Sherstinsky, 2020). The recurrent nature of LSTM allows the maintenance of hidden states over time, rendering them suitable for modeling sequences and time series data (Yu et al., 2019). LSTMs can capture patterns, trends, and dependencies in the temporal aspect of the data, which are critical information for predicting the temperature distribution across timestamps.

Building upon the strengths of CNNs and LSTMs, Convolutional LSTMs (ConvLSTM) have a hybrid architecture that seamlessly combines the spatial feature extraction capabilities of CNNs with the LSTM-like memory and sequential modeling capabilities (Shi et al., 2015). ConvLSTM operates by replacing the standard matrix multiplication in LSTM cells with convolutional operations. This fusion enables ConvLSTMs to simultaneously process spatial and temporal information, making them an ideal choice for tasks addressed in this paper, where 2D thermal images serve as inputs, and the goal is to predict a 2D temperature distribution evolving over time. The adoption of the ConvLSTM architecture equips the neural network with the capability to excel in the extraction of spatial features from thermal images through CNN-like operations, all while maintaining the capacity to model temporal dependencies using LSTM-like memory. Generally, the numbers of ConvLSMT modules and CNN modules depend on the complexity of tasks.

2.3.2. Physics-informed loss function

Referring to Section 2.1, a physics-informed loss function typically comprises two core elements: data-based loss and physics-based loss. The physics-based loss encompasses the residual of the PDE, quantifying the deviation between predictions and the PDE, along with the residual related to the boundary and initial conditions corresponding to the PDE.

The objective is to ensure that the framework's output adheres to the physics principles articulated by the PDE, as represented in Equations (10)–(12). To calculate temperature gradients across both time and space, the temperature distribution must be discretized into finite locations. This is achieved by subdividing the computation domain Ω into $m \times n$ cells with steps denoted as h. This discretization process is considered crucial when dealing with pixelized data, such as thermal images. Drawing inspiration from the finite difference method, we utilize differential approximations to compute the derivative terms in Equation (10).

$$\frac{\partial^2 T}{\partial x^2} \cong \frac{1}{h^2}[T(x_i+h,y_i) - 2T(x_i,y_i) + T(x_i-h,y_i)] \tag{13}$$

$$\frac{\partial^2 T}{\partial y^2} \cong \frac{1}{h^2}[T(x_i,y_i+h) - 2T(x_i,y_i) + T(x_i,y_i-h)] \tag{14}$$

The PDE loss can be formulated using the difference equations. Based on Equations (13) and (14), we derive the difference equation for Equation (10) as follows:

$$R\left(x_i,y_j\right) = -\rho C_p \frac{\left(T\left(x_i,y_j\right) - T_{prev}\left(x_i,y_j\right)\right)}{\Delta t} + \frac{1}{h^2}k\left(T\left(x_i+h,y_j\right) + T\left(x_i-h,y_j\right) + T\left(x_i,y_j+h\right) + T\left(x_i,y_j-h\right) - 4T\left(x_i,y_j\right)\right), x \in \Omega, t \in [0, t_{end}] \tag{15}$$

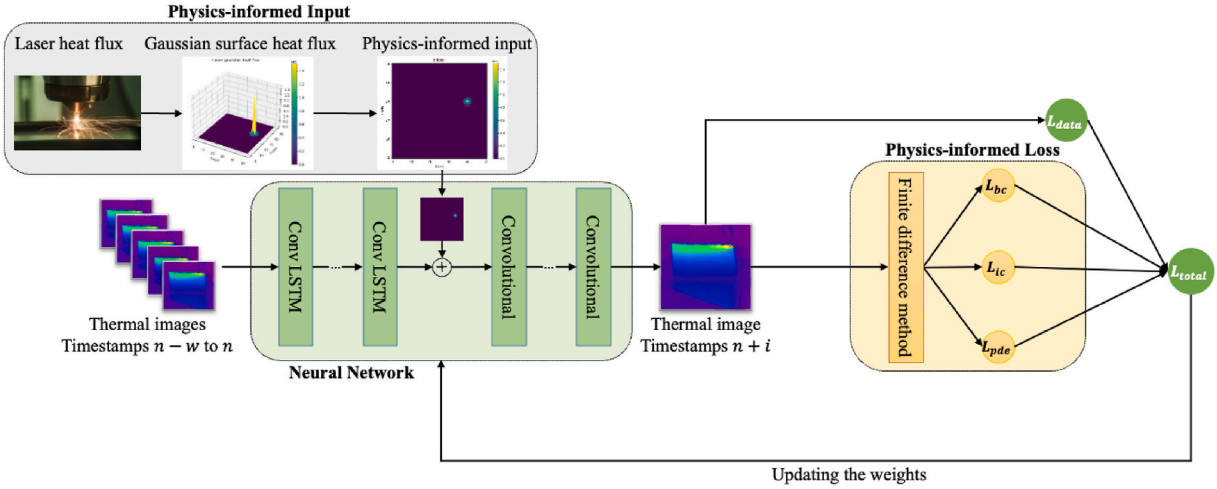

Fig. 3. Overview of PI-ConvLSTM framework with its components: the neural network, PI-input, and PI-loss.

where $T(x_i, y_i)$ is the temperature of the pixel at (x_i, y_i) in the 2D predicted temperature field and $T_{prev}\left(x_i, y_j\right)$ is the temperature of the pixel at (x_i, y_i) for the previous timestamp. As the framework's outputs are high-dimensional images, the residual for each output is structured as follows:

$$Res_{pde} = \begin{bmatrix} R\left(x_0, y_0\right) & \cdots & R\left(x_n, y_0\right) \\ \vdots & \ddots & \vdots \\ R\left(x_0, y_m\right) & \cdots & R\left(x_n, y_m\right) \end{bmatrix} \tag{16}$$

In an ideal situation, the framework's output temperatures should drive Res_{pde} to approach zero. Therefore, the PDE loss for the PI-ConvLSTM is formulated as:

$$L_{pde} = \frac{1}{N_p} \sum_{i=1}^{N_p} Res(i)_{pde}^2 \tag{17}$$

where N_p is the number of thermal images used to train the framework. The losses associated with initial and boundary conditions remain consistent with the explanations provided in Section 2.1.

2.3.3. Physics-informed input

In this section, the third component of the PI-ConvLSTM framework is introduced. Thus far, we have discussed the neural network architecture for predicting 2D temperature fields and explored the design of a specialized physics-based loss function. To improve the adaptability of our modeling approach for various manufacturing scenarios, we include important process parameters associated with the laser heat source.

Parameters such as laser power, laser absorptivity, beam radius, and laser location are deemed influential in thermal modeling for laser-based metal AM processes (Karmiris-Obratański et al., 2022; Siahvashi et al., 2021). Instead of directly providing these parameters as raw features to the model and expecting it to deduce their intricate relationship with temperature, we opt for a more informed strategy. We create an auxiliary physics-informed input, an intermediate feature that embeds meaningful physics knowledge related to the heat input, and incorporate it into a hidden layer of the neural network. This intermediate feature acts as a higher-level parameter that combines the influences of the mentioned process parameters. In our case, the selected higher-level parameter is the laser heat flux. The concept is to integrate information about the laser heat flux into the historical thermal information within the neural network to enhance the modeling process. In this study, we estimate the laser heat flux using a Gaussian surface heat flux model. The process of crafting this physics-informed input is detailed as follows: firstly, the heat flux for each point on the layer subjected to the laser's application is calculated as expressed in Equation (18):

$$q_{laser}(x, y) = -\frac{2\eta P}{\pi r_{beam}^2} \exp\left(\frac{2d^2}{r_{beam}^2}\right) \tag{18}$$

Here, η represents the laser absorptivity, P corresponds to the laser power, r_{beam} stands for the laser beam radius, and d represents the distance from the point (x, y) to the laser center. Subsequently, we aggregate the input heat flux across the entire layer where the laser is applied, resulting in the formation of the heat flux matrix q_{laser}, as shown in Equation (19):

$$q_{laser} = \begin{bmatrix} q_{laser}\left(x_0, y_0\right) & \cdots & q_{laser}\left(x_n, y_0\right) \\ \vdots & \ddots & \vdots \\ q_{laser}\left(x_0, y_m\right) & \cdots & q_{laser}\left(x_n, y_m\right) \end{bmatrix} \tag{19}$$

Each element within the matrix q_{laser} signifies the heat flux at a specific location on the layer where the laser is applied. Fig. 4 illustrates an instance of laser application on a surface, modeled using the Gaussian surface heat flux, along with its corresponding q_{laser} matrix. After the q_{laser} matrix is generated, it is introduced into the neural network following the ConvLSTM layers. At this stage, the ConvLSTM layers have processed the sequence of 2D thermal images and condensed the temporal patterns into a single 2D tensor. The idea is to leverage the temporal information captured by the ConvLSTM and then introduce the physics-informed input in a way that parallels how numerical models solve temperature fields using PDEs. Specifically, the laser heat flux matrix, which represents the heat input to the system, is added to this 2D tensor output from the ConvLSTM layers.

This step aims to incorporate the physical process of heat transfer after analyzing the temporal evolution of the temperature data. By adding the physics-informed input at this stage, the model integrates both data-driven insights from past temperature fields and the physically modeled heat input from the laser. This approach is designed to help the model better capture both the complex temporal patterns in the data and the underlying physics governing heat transfer, resulting in predictions of the temperature field that are more aligned with real-world thermal behavior.

3. Applications

In this section, we evaluate the practical performance and adaptability of the PI-ConvLSTM framework through two distinct applications. The first application (Section 3.1) focuses on assessing the

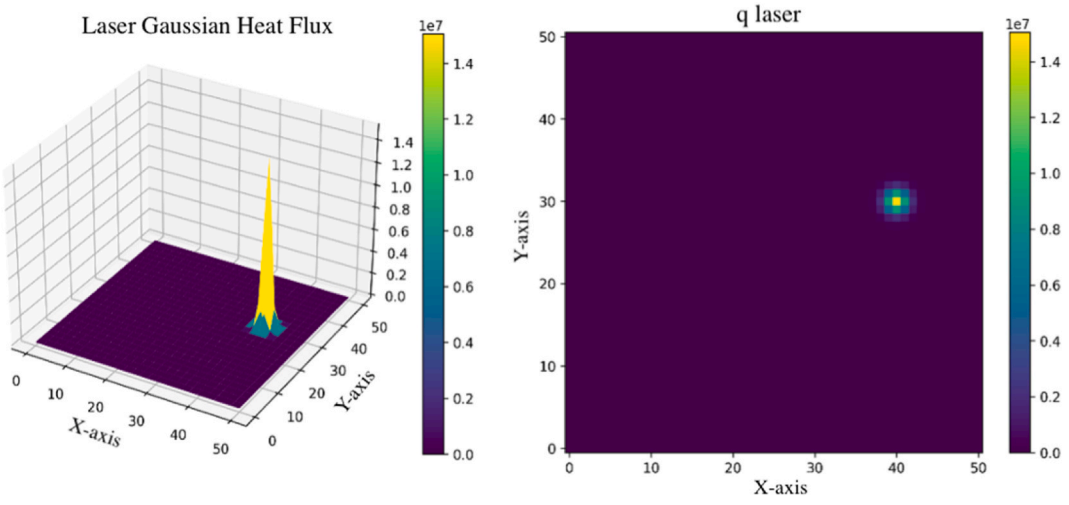

Fig. 4. Gaussian heat flux on a surface (left) and its corresponding q_{laser} matrix (right).

framework's ability to predict the 2D temperature field in a thin wall during a metal AM process, using experimental data from the literature. This scenario highlights the method's performance in terms of accuracy and reliability when applied to real-world, experimentally obtained data.

The second application (Section 3.2) demonstrates the framework's flexibility in modeling different processes with varying geometries and deposition patterns, with minimal alterations in the modeling approach. This stands out from other works that often require specialized modeling schemes based on hand-picked features specific to the studied process. In this case, the framework predicts the 2D temperature field for the actively printed layer of cylindrical and cubic geometries using simulation data. Unlike Application 1 that predicts temperatures for future layers throughout the process, Application 2 focuses on within-layer temperature prediction without predicting future layers.

3.1. 2D-temperature field prediction of a thin wall

In this section, we apply the PI-ConvLSTM framework to predict the 2D temperature field in a thin wall during a metal AM process. This application demonstrates the framework's ability to deliver accurate predictions using a small set of experimental data—specifically, 2400 infrared (IR) images—obtained from the literature. The goal is to assess the framework's performance when working with limited in-situ data, showcasing its robustness in achieving accurate predictions with a constrained dataset. Additionally, we discuss the impact of incorporating physics knowledge—through the PI input and PI loss function—into the neural network architecture. By focusing on a relatively simple geometry, this scenario provides a clear assessment of how well the model can predict temperature fields based on experimental data, while emphasizing the value of added physics knowledge in enhancing prediction accuracy.

3.1.1. Dataset and experimental setup

In the first application, we use the infra-red images taken during the Laser Metal Deposition process (LMD) for printing 60-layer Ti-6Al-4V thin-walled structures, provided by Marshall et al. (2016a). These data are measured by an IR camera, which is a part of the OPTOMEC Laser Engineered Net Shaping (LENS) 750 printer. The system setup is shown in Fig. 5. The thin wall was constructed at an orientation such that one of its sides was fully in-view by the IR camera. The data of the IR camera are output to comma separated value (CSV) files, each of which contains a 320 × 240 (width × height) matrix of temperature values. In total, 2760 thermal images are captured by the IR camera during the deposition process. These images undergo processing which includes cropping the images to focus on the region of interest, rotating them to align with a standard orientation, and normalizing the pixel values to a consistent scale.

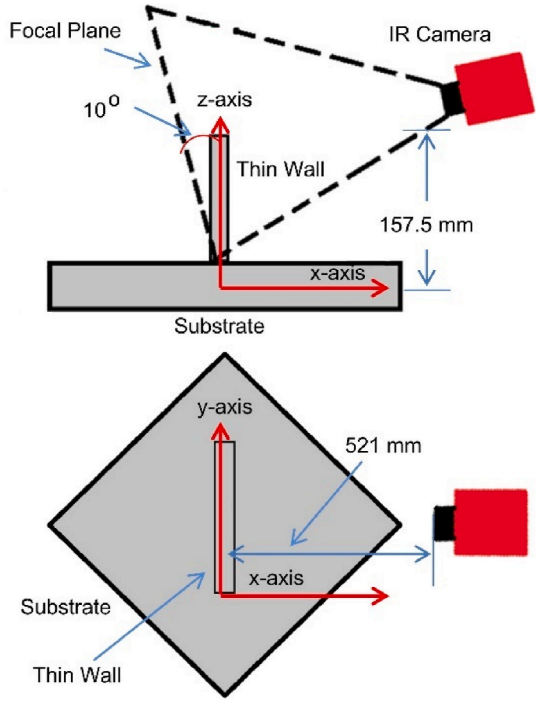

Fig. 5. Side view (top) and aerial view (bottom) of IR camera and its orientation with respect to the substrate and thin wall within the build chamber (Marshall et al., 2016b).

Processed images are then organized so that a sequence of w images forms one input, with the subsequent image corresponding to the next timestamp as the output. For instance, images from timestamp 100 to timestamp $(100 + w)$ serve as input to the framework, predicting the output image for timestamp $(100 + w + 1)$. As mentioned in Section 2.3, w serves as the window size for inputs and is determined through hyperparameter tuning.

3.1.2. PI-ConvLSTM framework for full-field temperature prediction

The developed PI-ConvLSTM framework serves as a tool for predicting the full temperature field for the ith future timestamp based on thermal images captured at previous timestamps. In this specific application, we simplify the model by assuming that temperature remains uniform throughout the material's thickness, thus allowing us to disregard solid heat transfer in the through-the-thickness direction (i.e., perpendicular to the surface of the thin wall, as shown in Fig. 5). This simplification transforms the heat transfer problem within the thin wall into a 2D case. In this revised model, we treat the convective and radiative heat flux occurring on the two surfaces of the wall parallel to the yz plane as a heat source term. This leads to the following expression of Equation (10):

$$\rho C_p \frac{\partial(T)}{\partial t} - k\left(\frac{\partial^2 T}{\partial x^2} + \frac{\partial^2 T}{\partial y^2}\right) + \frac{h}{w}(T - T_{amb}) + \frac{\sigma\varepsilon}{w}\left(T^4 - {T_{amb}}^4\right) = 0 \tag{20}$$

Here, w represents the thickness of the wall. The boundary conditions specified in Equation (11) are still valid for the left and right boundaries of the 2D wall, and Equation (12) applies to the upper surface of the wall.

The input to the model consists of a sequence of IR images representing the temperature field at previous timestamps, along with physics-informed features such as laser heat flux. These inputs enable the model to predict the full-field temperature distribution for the next timestamp. The output is a 2D temperature field corresponding to the future time step, which captures the temperature variations across the entire surface of the part being printed.

The neural network architecture includes three ConvLSTM layers followed by two Convolutional layers, each equipped with 10 filters and ReLU activation. The ConvLSTM layers are responsible for capturing the spatiotemporal dependencies in the temperature field sequence, while the Convolutional layers refine the spatial features to improve the accuracy of the temperature predictions. The hyperparameters, including the number of layers and filters, are selected through a trial-and-error process, testing configurations from {2, 3, 4} layers and {8, 10, 12} filters, with 10 filters and three layers providing the best performance. The weights of the loss terms are set proportionally to their initial values to maintain a balanced scale. This ensures that each terms contributes equally during training, preventing one from dominating and skewing the model's learning process.

The model is implemented using Python and TensorFlow, and training is conducted on an Intel Core i7 CPU with 16 GB of RAM. The training process spans 40 epochs, as the model converged within this range without significant improvements from further training, utilizing the Adam optimizer with a learning rate of 10^{-3}. The Adam optimizer is

selected for its computational efficiency and ability to handle sparse gradients. Training takes approximately 2.5 h. Once trained, the model demonstrates real-time inference capabilities, with each temperature field prediction for the next time step taking a fraction of a second, making it suitable for real-time temperature field prediction in metal AM processes.

3.1.3. Results and discussion for full field temperature prediction

To assess the performance of the developed framework against experimental data, we utilize various evaluation metrics, including Mean Absolute Error (MAE), Mean Square Error (MSE), and Mean Absolute Percentage Error (MAPE). The use of these three metrics provides a comprehensive evaluation of the model's performance. MSE emphasizes overall accuracy with a focus on larger errors, while MAE treats all errors equally, and MAPE gauges relative accuracy by expressing errors as a percentage of actual values. This multi-metric approach ensures a nuanced understanding of precision, error magnitude, and percentage-wise accuracy, enhancing the overall assessment of the model.

$$MSE = \frac{1}{n \times m} \sum_{i=1}^{n} \sum_{j=1}^{m} \left(Y_{ij} - \widehat{Y}_{ij}\right)^2 \tag{21}$$

$$MAE = \frac{1}{n \times m} \sum_{i=1}^{n} \sum_{j=1}^{m} \left|Y_{ij} - \widehat{Y}_{ij}\right| \tag{22}$$

$$MAPE = \frac{1}{n \times m} \sum_{i=1}^{n} \sum_{j=1}^{m} \left|\frac{Y_{ij} - \widehat{Y}_{ij}}{Y_{ij}}\right| \tag{23}$$

where, Y_{ij} and $\widehat{Y}_{ij}$ represent the actual and predicted temperature fields for each element in the dataset respectively, with n and m denoting the number of rows and columns in the temperature matrix. These metrics assess individual errors. The overall error for validation dataset is obtained by averaging these individual errors, providing an evaluation of the entire validation dataset.

- **Effect of window size on prediction error**

In Section 2.3, the window size is identified as a hyperparameter to be determined through tuning. To find the most accurate window size, a range of window sizes from $w = 1$ to 6 is tested, and the outcomes are depicted in Fig. 6. Based on these results, a window size of five demonstrates the lowest MSE, hence is chosen as the number of previous timestamps to use as input.

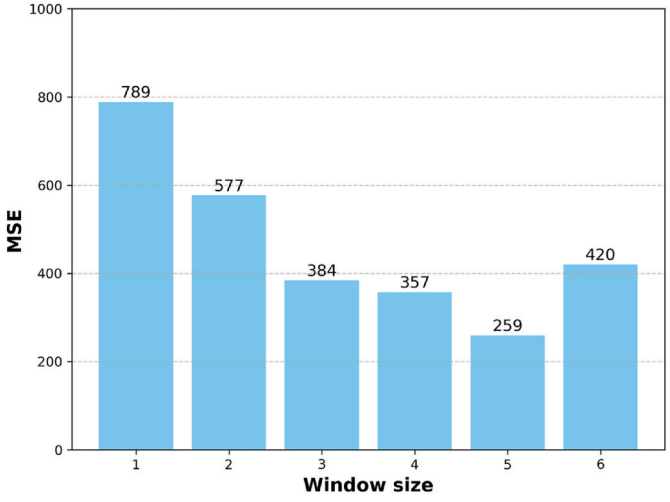

Fig. 6. MSE on the validation dataset for different window sizes.

- **2D temperature prediction results**

Fig. 7 shows a comparison between the predicted temperature field made by the PI-ConvLSTM framework and the actual experiment results at different times. It also displays the difference between the predicted and experimental data. While most areas in the prediction closely match the real results, accuracy slightly decreases around the melt pool region. This reduced accuracy can be attributed to the intricate and complex nature of the melt pool area. The area's swift temperature fluctuations, complex phase transitions, and dynamic material behavior present challenges for precise prediction due to their highly nonlinear and transient characteristics. Moreover, the melt pool is subject to diverse boundary conditions, such as extreme temperatures and rapid thermal gradients, which, if not accurately represented, significantly impact the model's predictive accuracy within this region.

- **Comparison with State-of-the-Art Models**

To assess the effectiveness of the proposed PI-ConvLSTM framework, we compared it against two state-of-the-art models: a 3D Convolutional Neural Network (3D CNN) and a U-Net. The 3D CNN model processes spatiotemporal data by applying 3D convolutions across both spatial and temporal dimensions simultaneously, effectively learning joint features that capture temporal dynamics and spatial correlations. This makes the 3D CNN a natural candidate for sequential prediction tasks like temperature field forecasting, where the temporal evolution of the field is critical. The U-Net model is a widely recognized benchmark for spatial prediction tasks, known for its encoder-decoder architecture with skip connections that efficiently preserve spatial details. To adapt it for sequential temperature field prediction, we restructured the input data by stacking temporal frames along the channel dimension, enabling the model to process sequential information as multi-channel spatial data.

The 3D CNN architecture consists of three 3D convolutional layers with 16, 16, and 8 filters, respectively, using a kernel size of (2, 3, 3), followed by batch normalization. A Lambda layer averages over the temporal dimension, reducing the input to a 2D spatial representation, which is further processed by two 2D convolutional layers with 16 filters each and a final 2D convolutional layer for output generation.

The U-Net, a benchmark model for spatial prediction tasks, was adapted for sequential prediction by restructuring the input data to stack temporal frames along the channel dimension. Its encoder-decoder architecture includes two convolutional layers per level in the encoder and decoder, each with 64 filters, and a bottleneck with 128 filters. Skip connections link the encoder and decoder, preserving spatial details for accurate predictions. Both models were tuned through trial-and-error to ensure fair comparison with the proposed framework.

The results of the comparison between the proposed PI-ConvLSTM framework, the 3D CNN, and the U-Net models are illustrated in Fig. 8 and summarized in Table 2. Fig. 8 presents the evolution of validation loss for each model across 20 training epochs, highlighting the performance trends over time. The PI-ConvLSTM achieves the lowest loss throughout the training process, converging rapidly within the first few epochs. The 3D CNN exhibits a slower convergence with moderately higher loss values, while the U-Net struggles significantly, maintaining the highest validation loss across all epochs. This trend underscores the challenges faced by U-Net in handling sequential temperature field prediction tasks due to its lack of temporal processing capabilities.

The performance metrics presented in Table 2 further reinforce the superiority of the PI-ConvLSTM. By leveraging physics-informed inputs and loss functions, the framework achieves lower errors compared to the other models, showcasing its ability to effectively capture both spatial and temporal dependencies in the data. While the 3D CNN performs better than the U-Net, its lack of integration of physics-informed knowledge limits its predictive accuracy when compared to the PI-ConvLSTM. The U-Net, despite its strength in spatial prediction tasks, is outperformed due to its architectural limitations in processing

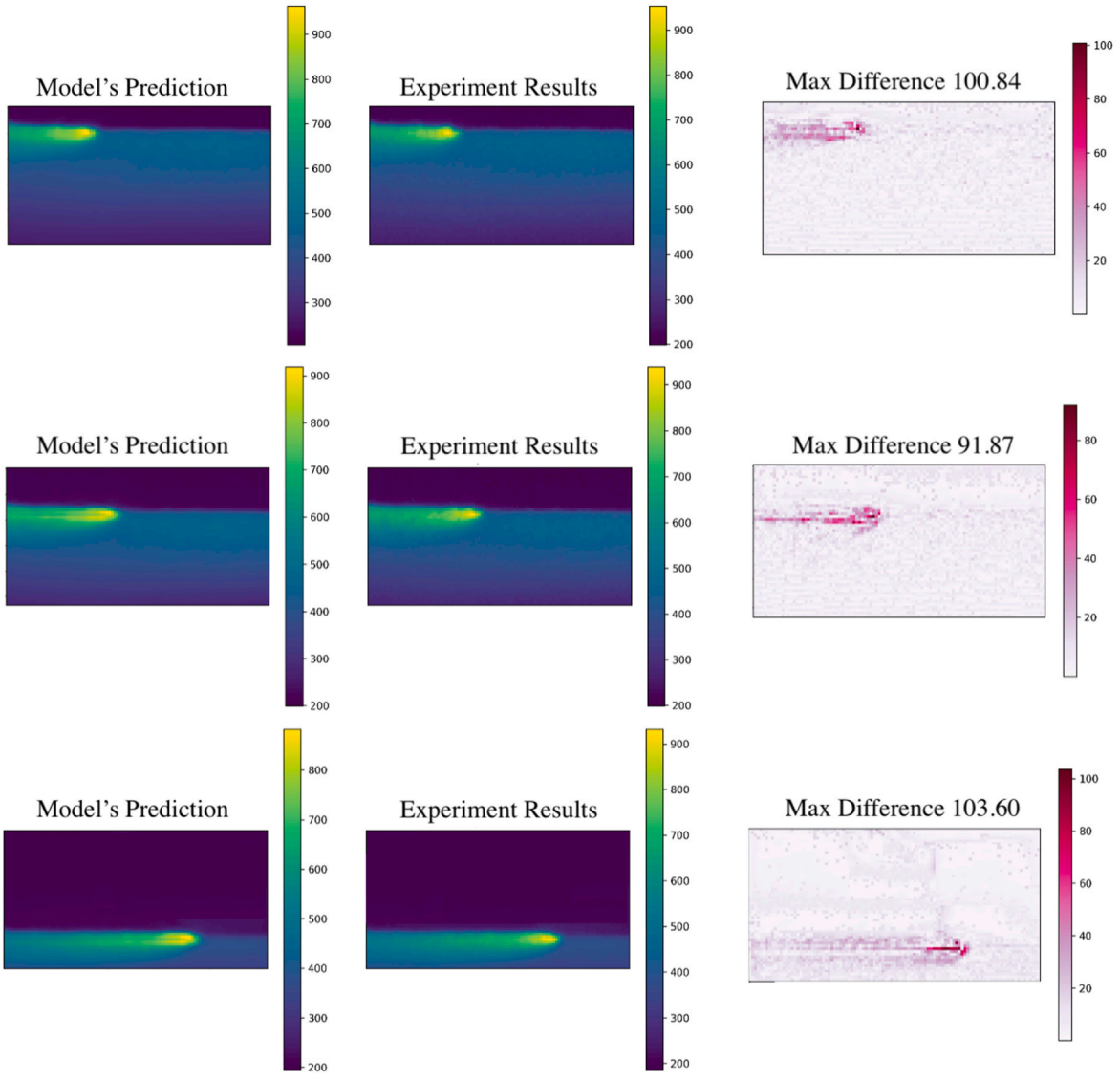

Fig. 7. Comparison of the temperature field from the framework prediction and experimental results in a cross-Sectional view (top: timestamp = 2300 (t = 391s), middle: timestamp = 1900 (t = 270s), below: timestamp = 900 (t = 117s)).

sequential data.

Additionally, all models demonstrated computational efficiency, with training times of approximately 20 min for 20 epochs and inference times in milliseconds on a Tesla V100 GPU with 40 GB memory, making them suitable for in-situ applications. However, the superior accuracy and faster convergence of the PI-ConvLSTM clearly establish it as the most effective framework among the three for temperature field prediction in metal AM processes.

- **Effect of Physics-informed components on prediction error**

As previously described, the PI-ConvLSTM framework consists of three integral components: the PI loss, the PI input, and a neural network. In order to evaluate the influence of each component, we conducted multiple experiments. We trained the model for 40 epochs in various configurations: one included both the PI loss and PI input, another solely used the PI loss, a third model only implemented the PI input, and the final model (ML-only model) excluded any PI components. For all configurations, the input to the model was a sequence of previous thermal images. However, the PI input, which incorporates features derived from the laser heat flux, was only included in configurations explicitly using physics-informed components. The obtained results, shown in Table 3, indicated that the model utilizing solely the PI input excelled over the ML-only model across various evaluation metrics. Additionally, the model incorporating the PI loss displayed a strong performance, benefiting from its ability to integrate the PDE, boundary condition, and initial condition to enhance robustness against existing noises within the data. Notably, the model that combined both the PI loss and PI input (i.e., PI-ConvLSTM) outperformed other configurations across all evaluation metrics. This superiority is due to its

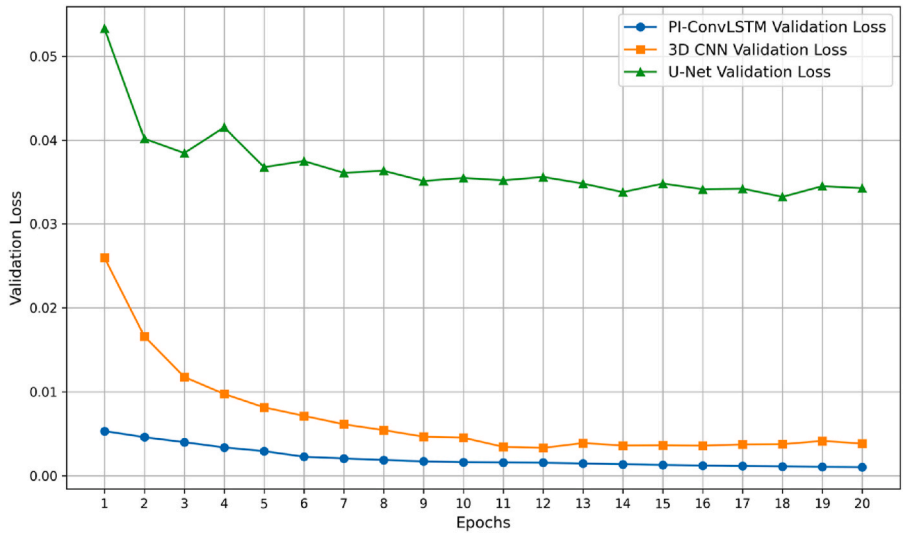

Fig. 8. Evolution of validation loss for PI-ConvLSTM, 3D CNN, and U-Net during the training process.

Table 2
Performance metrics comparison of PI-ConvLSTM, 3D CNN, and U-Net.

Model	MSE	MAE	MAPE
PI-ConvLSTM	473	13.7	2.84 %
3D CNN	1606	15.8	4.66 %
U-Net	16592	80.8	18.16 %

Table 3
The results for PI-ConvLSTM framework with different configurations.

Model Variation	MSE	MAE	MAPE
ML Only	1967	57.5	14.39 %
PI input	1176	48.9	11.14 %
PI loss	302	13.1	2.73 %
PI input + PI loss	273	11.3	2.15 %

comprehensive integration of physics principles through the PI loss, inclusion of process parameters like laser heat flux via the PI input, and utilization of experimental information for comprehensive field temperature prediction.

3.2. 2D-temperature field prediction of a cylinder and a cube

The second application shifts the focus to testing the adaptability of the PI-ConvLSTM framework across different metal AM processes. Here, we predict the 2D temperature field for the currently printed layer (within-layer prediction) in cylindrical and cubic geometries using simulation data. The purpose of this application is to demonstrate the framework's flexibility in modeling different geometries and deposition patterns with minimal alteration to the overall modeling approach, contrasting with other works that often require hand-picked, process-specific features. This application evaluates the framework's ability to handle diverse AM processes, providing insight into its robustness when dealing with simulation data for more complex shapes.

3.2.1. Dataset and simulation setup

In the second application, we employ the PI-ConvLSTM framework to predict 2D temperature field for the currently printed layer of a cylinder and a cubic shape part. Within this section, to test the adaptability

Table 4
Material properties used in the simulation.

Parameter	Value	Unit
Density, $\boldsymbol{\rho}$	$7915 - 0.59 \times T$	kg/m^3
Heat conductivity, $\boldsymbol{k}$	$12.6 + 0.015 \times T$	$W/m\,^\circ C$
Heat capacity, $\boldsymbol{C_p}$	$496.5 + 0.133 \times T$	$j/kg\,^\circ C$
Convection coefficient, $\boldsymbol{h}$	10	$W/m^2\,^\circ C$
Emissivity, $\boldsymbol{\varepsilon}$	0.3	–

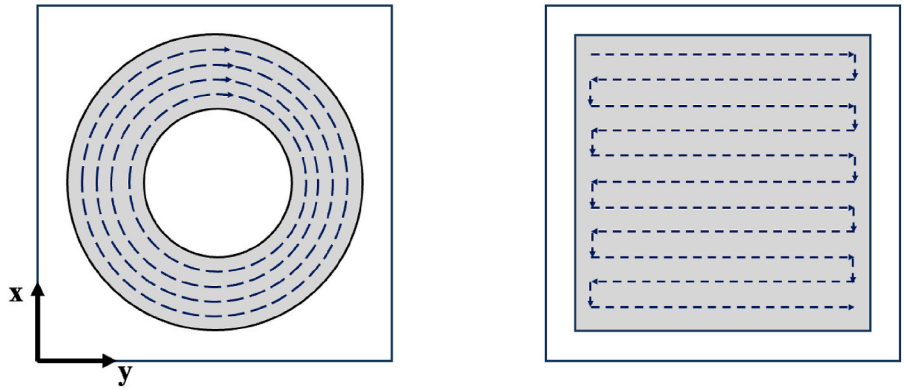

Fig. 9. Illustrations of geometry and deposition patterns for 2D temperature field prediction. The grey lines indicate the base, the black lines indicate the deposition geometry, and the dashed arrows indicate the direction of the laser.

of the framework, two distinct geometries with corresponding deposition patterns have been selected. Cylindrical and cubic geometries, widely used in the industry are chosen to serve as the foundation for the study. An overview of these geometries and deposition patterns can be observed in Fig. 9.

We utilized the pre-built formulations and integrated physics within the ANSYS AM DED process module, specifically crafted for the Directed Energy Deposition process for the simulation of the process. In the simulations, the pass width and the layer thickness are set to maintain a consistent pass of 1 mm. Both the substrate and deposited parts are made from the 316 stainless steel. A summary of material properties can be found in Table 4, with a linear correlation assumed between material properties and temperature throughout the simulation process. Our study focuses on multi-layer fabrications, with each layer adhering to the same printing pattern and geometry to systematically examine thermal behavior and ensure consistency across layers. The cubic part consists of 8 layers, while the cylindrical part has 10 layers. The deposition path is defined using a G-code file, which specifies the material deposition trajectory over time. For the cylindrical geometry, the circular movements are approximated by a high-dimensional polygon to represent the curved surface within the constraints of the G-code format.

The boundary conditions are designed to simulate realistic printing conditions. Surfaces exposed to ambient air are subject to convection and radiation, with the convection coefficient set to one. Heat conduction is applied at the substrate-part interface, using a heat conductivity coefficient based on the material properties of 316 stainless steel. The software automatically identifies contact surfaces and deposition layers according to the geometry and G-code file provided. The initial temperature of the substrate and ambient temperature is consistently set at 23 °C. The deposition speed stands at 10 mm/s for the cylinder and 7 mm/s for the cubic part. The ANSYS AM DED simulation employs an inactive activation strategy, where elements representing the deposited material are activated following the deposition sequence at specific times. Upon activation, these elements are assigned a temperature defined as the "process temperature". In this scenario, the element activation temperatures are set at 1800 °C for the cubic part and 2400 °C for the cylindrical part. These values are higher than the typical melting point of the material. Experimental results for 316 stainless steel, as reported in studies (Bernauer et al., 2022; Chaurasia et al., 2023), indicate that the melt pool temperature typically ranges from 1500 °C to 1800 °C. To account for the elevated temperatures at the center of the melt pool, where the laser directly interacts with the material, we selected 1800 °C and a higher value of 2400 °C to accurately capture the increased thermal accumulation in the central region of the melt pool. Notably, the simulation does not model the laser heat flux directly. Instead, in the simulation setup, the process temperature is input directly, bypassing the need to explicitly define the laser heat flux as a parameter. As a result, the laser power is treated as a trainable parameter, with its initial value set to match the experimental data. During training, this value is iteratively adjusted to minimize the model's error, allowing the model to infer the most appropriate laser power based on the available data. This allows the model to infer the laser power from the available data, rather than relying on a predefined or simulated value. Although the laser heat flux input is calculated as a function of the laser power P, this input, like other features, is normalized to a range of 0–1 during the preprocessing stage for a more stable training.

In each dataset, the transient temperature values for all nodes are recorded. To efficiently extract and process these results, we developed a Python script integrated within the ANSYS environment. This script retrieves temperature values for all nodes at each timestamp and exports them to individual text files, each named according to its corresponding timestamp. Post-simulation, we process these files by matching node IDs with their corresponding coordinates to construct a point-wise temperature dataset. This dataset is then filtered to extract specific points of interest, focusing on the 2D temperature fields of the currently deposited layer and the layer immediately below it for each timestamp.

The preprocessed data is structured into input-output pairs for training and validation of our machine learning framework: a sequence of the 2D temperature field for the currently printed layer and the layer below, along with the physics-informed laser heat flux are used as inputs, with the corresponding output representing the 2D temperature field of the currently printed layer for the next timestamp within the same layer as input. Each simulation comprises roughly 16,000 timestamps, resulting in approximately 16,000 input-output pairs extracted for training and validating the framework for each of the geometries. 80 % of the data is allocated for training, while the remaining 20 % is set for validation.

3.2.2. PI-ConvLSTM framework for 2D temperature field prediction

In this application, our focus lies on predicting the 2D temperature field for the currently printed layer. To achieve this, the model exclusively integrates the boundary conditions related to the top surface, where the laser is applied. Therefore, Equation (12) is included in the PI loss function, which can be represented as:

$$L_{total} = w_b L_{bc} + w_i L_{ic} + w_d L_{data} \tag{24}$$

w_b, w_i and w_d are weights set proportionally to ensure a balanced scale among the various terms in the loss function, contributing to the model's enhanced training robustness. This tailored approach allows the model to work with image-based inputs for various geometries. Due to the complexity of the geometry and availability of more training data, a more sophisticated model is used for the second application. This approach employs a model equipped with six ConvLSTM layers and four Convolutional layers, each utilizing 20 filters and ReLU activation, to predict the 2D temperature field for both cylindrical and cubic parts. The laser heat flux distribution for each geometry at every timestamp is integrated into the model after the ConvLSTM layers. Each geometry undergoes separate training sessions consisting of 12 epochs, utilizing the Adam optimizer with a learning rate of 10^{-3}. The number of epochs was chosen as the model reached convergence within this range, and additional epochs did not significantly improve the results. Due to the increased model complexity and the larger dataset, training takes approximately 2 h per geometry on the same Intel Core i7 CPU with 16 GB of RAM, even though fewer epochs are required compared to Application 1.

3.2.3. Results and discussion for 2D temperature field prediction

- **Effect of the window size on the prediction error**

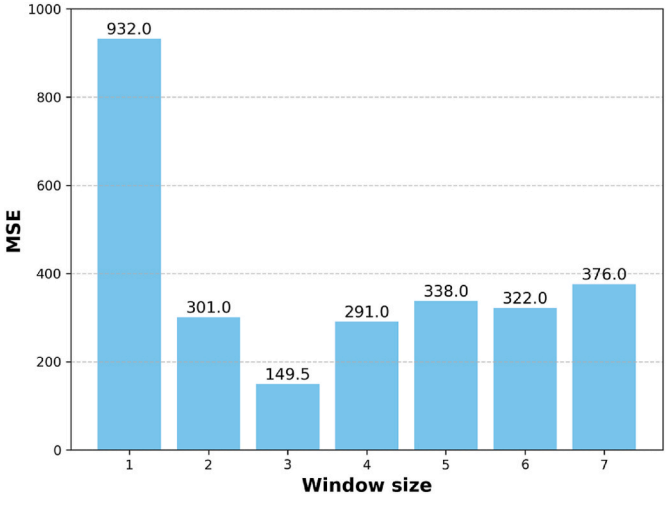

Fig. 10. MSE on the validation dataset for different window sizes.

Table 5
Prediction results of 2D temperature fields using the PI-ConvLSTM framework.

Geometry-deposition pattern	MSE	MAE	MAPE
Cylinder-Spiral	149.5	7.62	0.67 %
Cube-ZigZag	115.0	6.85	0.74 %

To determine the optimal window size for 2D temperature field prediction, multiple window sizes from $w = 1$ to 7 were tested. From the outcomes detailed in Fig. 10, a window size of three was found to yield the lowest MSE, and subsequently selected as the number of preceding time steps for the model input.

- **2D temperature prediction results**

Consecutively, the results for 2D temperature field prediction for the cylinder and cubic parts are presented in Table 5. These findings reveal a strong concordance between the predictions generated by the PI-ConvLSTM framework and the simulation results. The predictions demonstrate less than 1 % MAPE and an approximate MAE of 7 °C for both geometries and deposition patterns. While the relative error in cylinder geometry is lower than in the cube, the increased temperature range in this process contributes to generally higher MSE and MAE for the cylinder, with the squared error notably intensifying in higher temperature ranges, particularly in the MSE. The accuracies in both cases are notably satisfactory, indicating the robustness and adaptability of the framework for temperature predictions across diverse process parameters, geometries, and deposition patterns.

In comparison, recent studies (Hosseini et al., 2023; Li et al., 2023; Xie et al., 2022b) have achieved relative errors ranging from 1 % to 4.5 % in temperature prediction tasks. However, these works focus solely on single-track scenarios and rely on extensive FEM-generated datasets, with one study using over 10 million FEM temperature points for training. Despite using far less training data, the PI-ConvLSTM framework achieves comparable or better accuracy while handling more complex geometries and deposition patterns.

Fig. 11 compares the predicted temperatures from the PI-ConvLSTM with simulated temperatures for both the cylinder and cube. The predicted temperatures match well with the actual temperatures in most areas, with differences typically below 20 °C. Closer to the melt pool, however, there are bigger differences, likely for reasons similar to those in Fig. 7. Notably, the model's predictions are less accurate for the

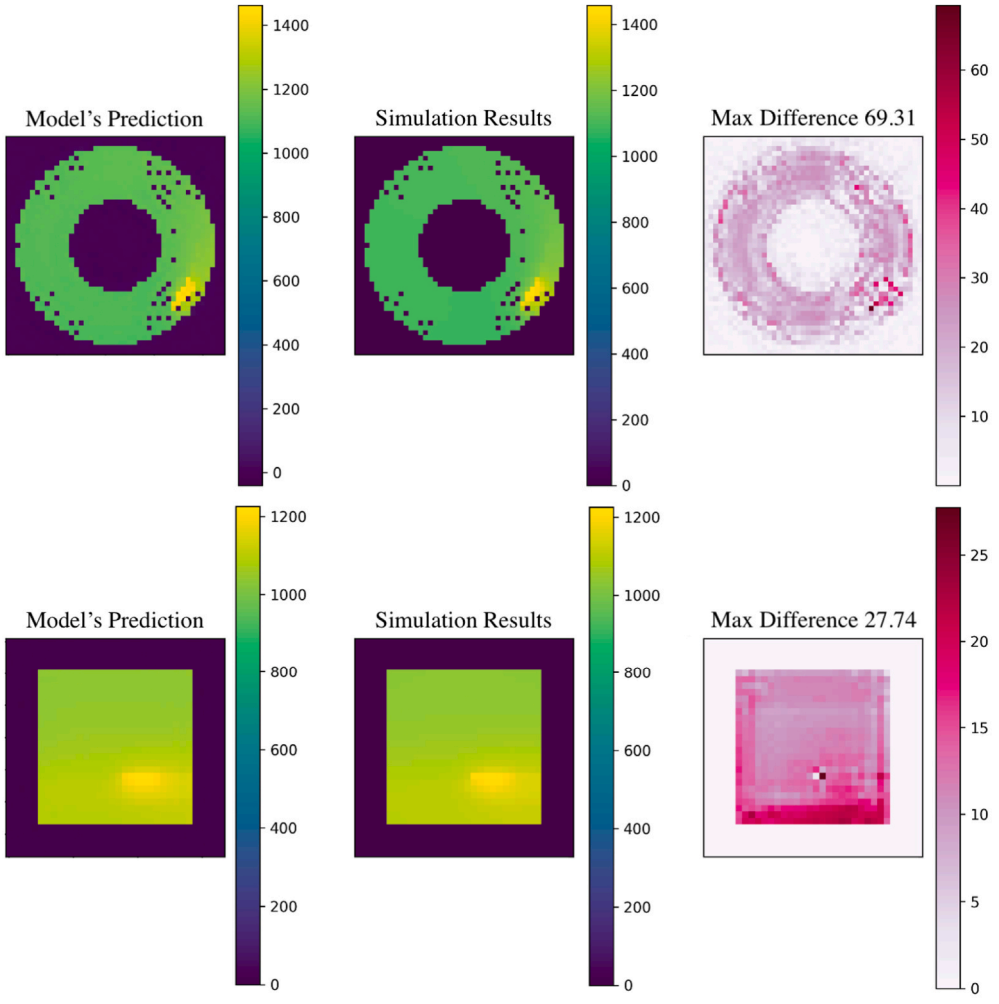

Fig. 11. Comparison of the temperature field from the framework prediction and simulation results in a top view (top – the cylindric part, bottom – the cubic part).

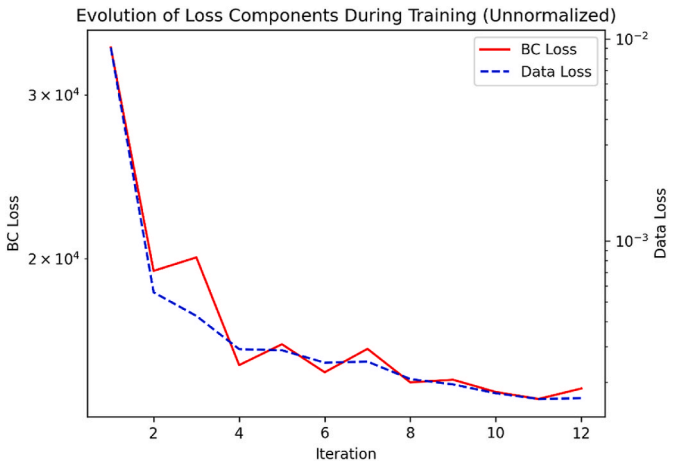

Fig. 12. Evolution of unweighted loss terms during the training process.

cylinder than for the cube, mainly because of the higher process temperature chosen for this geometry. Additionally, the more complicated pattern of material deposition in processing the cylinder may cause additional errors in modeling how the heat is transferred.

- **Evolution of loss terms through training**

To assess the framework's performance in data-based and physics-based aspects, Fig. 12 illustrates the evolution of boundary condition and data loss across the training process. The decreasing data loss over training suggests the model is adapting to the data. Boundary condition loss not converging to zero, however, suggests that while the physics-based constraints in Equation (12) provide valuable insights into the thermal behavior in the process, they might not be comprehensive in describing the entire thermal system. The convergence to a non-zero value implies that merely enforcing physics principles might not be adequate on their own to achieve the desired solution. Therefore, the combination of data loss with the underlying physics principles becomes imperative for a more accurate representation of the system dynamics.

- **Residual of physics-based loss function through training**

Fig. 13 demonstrates the variation in the residual matrix associated with the boundary condition loss as the training progresses, for a sample test input. Each matrix within the figure represents the residual values corresponding to a distinct iteration during the training of the model. These matrices depict the residuals across the surface of the dataset: brighter points denote higher residuals, while dark shades indicate lower residuals. Initially, in the early stages of training, the matrices predominantly exhibit higher residuals, signifying disparities between the model's predictions and the standards defined in the physics-based loss. As training progresses, the matrices gradually exhibit lower residuals, indicating improved alignment between the model's prediction and the governing physics principles (as represented by Equation (12)).

The upper left region of Fig. 13, however, consistently shows higher residual values, even in the later stages of training. This region

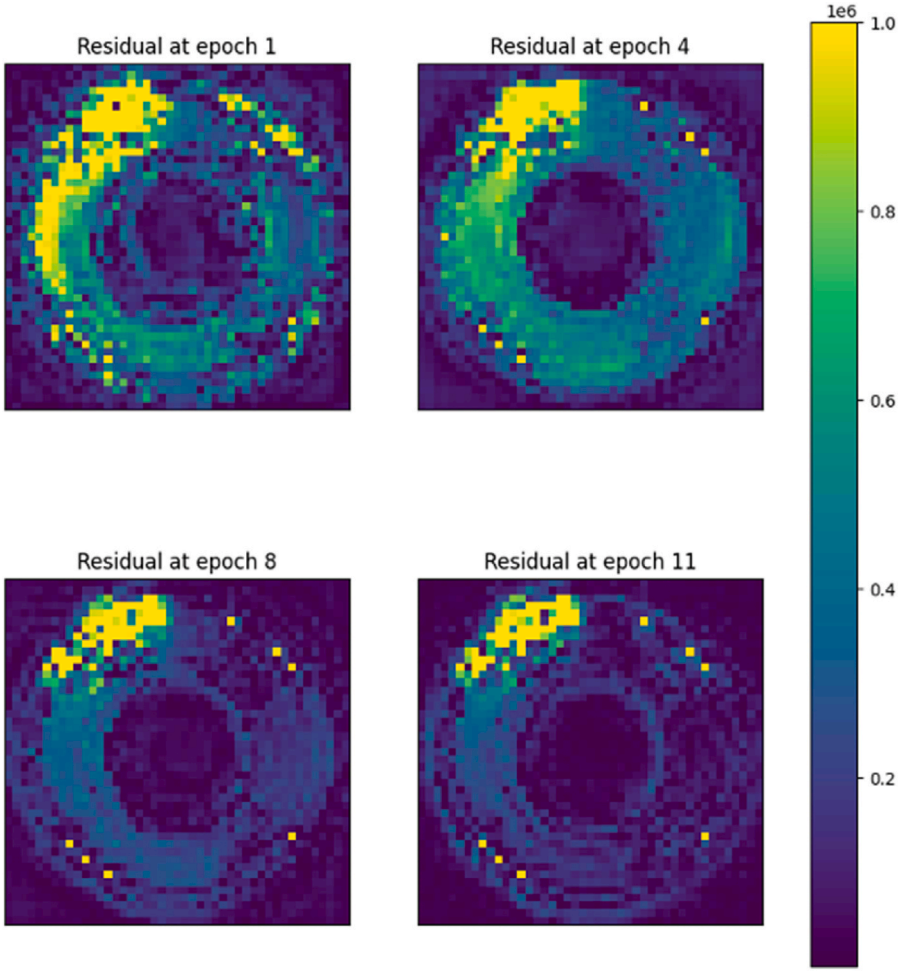

Fig. 13. Residual of the Boundary Condition loss during the training process.

corresponds to the melt pool area, where highly complex thermal behaviors occur, including rapid phase changes, evaporation, and convective flows such as the Marangoni effect (Ning et al., 2021; Saldi et al., 2024). These phenomena introduce intricate dynamics that are not fully captured by the simplified boundary condition in Equation (12).

This boundary condition accounts for heat transfer due to convection, radiation, and laser input, but it does not fully encapsulate the fluid dynamics and non-linear thermal gradients present in the melt pool. In particular, the Marangoni effect, driven by surface tension gradients, and the phase transitions occurring at the melt pool boundaries are not sufficiently described by the heat conduction and heat flux terms in Equation (12). Additionally, the complex radiative heat transfer near the highly dynamic melt pool surface introduces non-linearities that are difficult to capture with a simplified radiative loss term. These limitations contribute to the elevated residuals in this area, where the model struggles to fully capture the behavior of the rapidly changing temperature fields.

- **Effect of the number of training data**

To explore the influence of training data quantity on the framework's accuracy, the model was trained using 800, 3200, 5600, 8000, and 12500 pieces of training data. As illustrated in Fig. 14, a noteworthy finding emerged: achieving below 10 % error required just 3200 training samples, while obtaining less than 1 % error for predicting the next timestamp required 12,500 training samples. This result emphasizes the framework's efficiency in delivering accurate predictions with a limited dataset.

- **Prediction of extended timestamps**

In practical applications, the utility of the framework relies on its ability to not only predict the temperature field for the next timestamp but also for more extended future periods. To assess the accuracy of the framework in predicting later timestamps, two distinct approaches are considered. The first approach involves a rolling prediction, where the prediction for the timestamp $(t+1)$ serves as input for predicting $(t+2)$, and this process continues iteratively. In this approach, the hyperparameter i, representing the timestamp in the future for prediction, is set to 1, and the framework iteratively predicts the next timestamp. The second approach is a direct prediction of a future timestamp (e.g., $t+10$) by setting i to the desired prediction timestamp. For example, with $i = 10$, the framework predicts the thermal image (i.e., the 2D temperature field) for the 10th timestamp in the future.

The results for both approaches are depicted in Fig. 15(a) and (b). In the rolling approach, prediction errors remain below 8 % for timestamps up to the 10th, but its accuracy drastically decreases for timestamps beyond the 10th. As for the direct approach, prediction errors for $i = 10$, 20, 50, 100, and 200 are illustrated. The prediction error increases as we attempt to predict timestamps further in the future, although it remains lower than using the rolling approach. This difference arises because, in the rolling approach, where predictions for later timestamps depend on preceding ones, the error accumulates over time, limiting its effectiveness for predicting many timestamps in the future. Conversely, the direct approach avoids error accumulation, making it more useful for predicting timestamps far in the future.

However, if the focus is on understanding the dynamics of thermal behavior, the rolling approach can provide insights at a lower computational cost, as the direct approach necessitates training separate models for each timestamp i. In conclusion, for predicting the temperature field for longer timestamps in the future, the direct approach demonstrates a higher potential. However, if the objective is to comprehend the temporal dynamics of the temperature field, the rolling approach can yield results by training only a single model for the next timestamp (i.e., $i = 1$).

4. Insights, constraints, and prospects

The proposed framework demonstrates a capacity to predict the thermal field with a precision that yields an error rate below 3 % for the subsequent timestamp and below 7 % when forecasting up to the 50th timestamp for the cylinder part. This capability suggests its potential integration into control systems to facilitate corrective actions by adjusting process parameters to ensure process stability. The architecture of the ConvLSTM, along with the design of the loss function, offers flexibility in predicting temperature fields for different geometries and diverse deposition patterns through a single unified model, suggesting its potential in broader applications. Notably, its utility extends to systems requiring future timestamp predictions. This model can potentially substitute field-governing PDEs with the heat transfer PDE and laser heat flux employed in this study, allowing for wider applicability across various domains.

Despite these advancements, the framework faces inherent

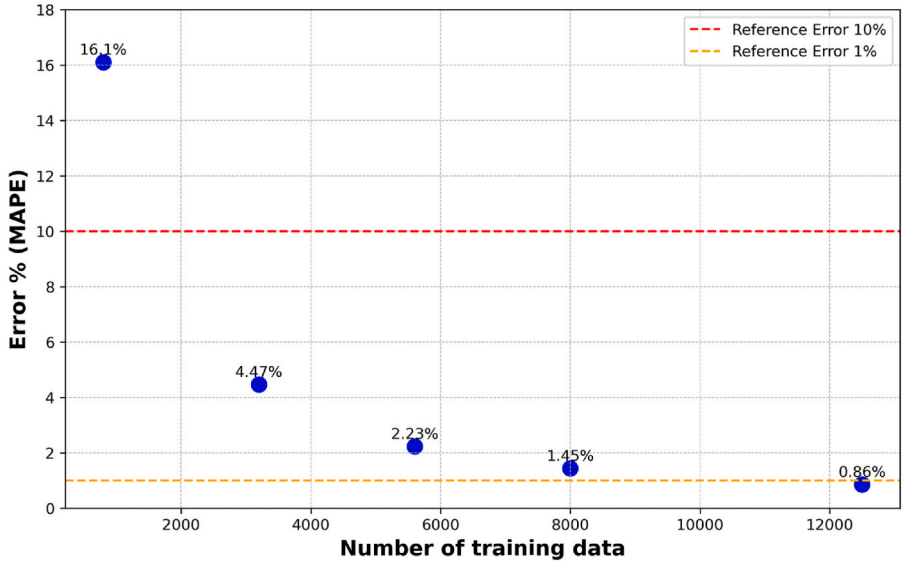

Fig. 14. PI-ConvLSTM prediction error with different numbers of training data.

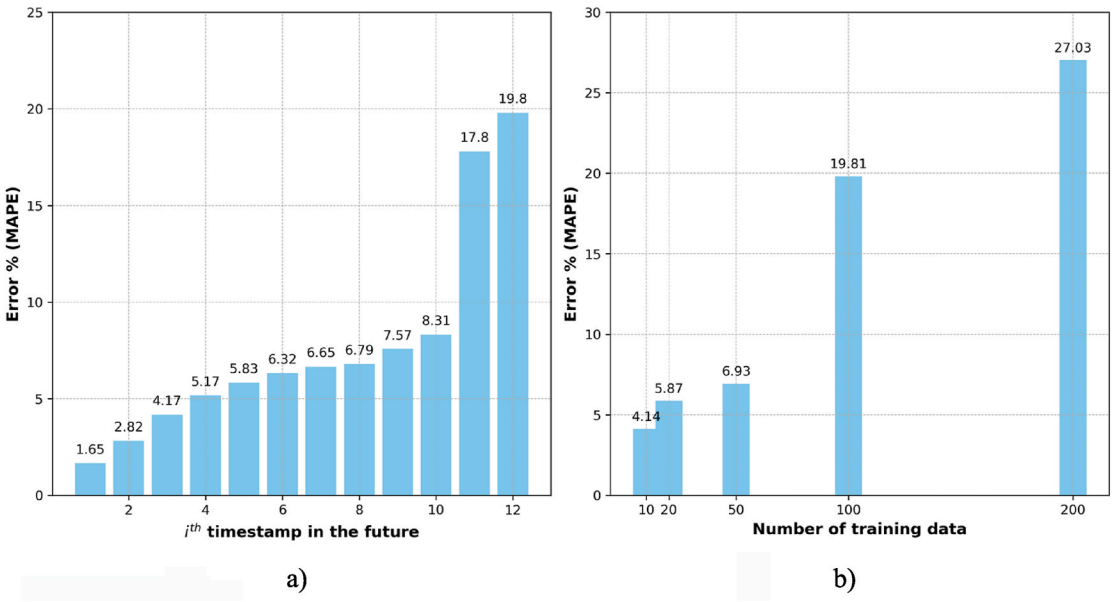

Fig. 15. a) Error for rolling prediction of the *i*th timestamp in the future b) Error for direct prediction of the *i*th timestamp in the future.

limitations. While it incorporates the heat transfer equation in the loss function, the physics-informed loss converges to a non-zero value, indicating the PDEs are not sufficient in describing the thermal behavior within the process, particularly in the melt pool area. The melt pool region, influenced by phenomena such as phase changes, the Marangoni effect, and non-linear thermal gradients, presents challenges that are not fully addressed by the current heat transfer principle incorporated into the framework. Additionally, in Application 2, the model is limited to within-layer temperature prediction and does not extend to predicting temperature in future layers. Furthermore, the resolution of the discretization, both spatially and temporally, significantly influences the accuracy of predictions. Lastly, the approach relies on in-situ temperature data acquisition through an infrared (IR) camera, which could be a practical constraint, limiting its applicability in processes without such sensors.

5. Conclusions

This study introduces the PI-ConvLSTM framework, a physics-informed neural network designed for real-time temperature field prediction in metal additive manufacturing (AM) processes. The framework employs transient heat transfer equations and a Gaussian surface heat flux model as physics-informed loss and input, respectively, for a neural network with convolutional and convolutional LSTM layers. The proposed approach predicts the temperature field for future timestamps using in-situ temperature field data from previous timestamps, along with a physics-informed input matrix that encodes process parameters in a physically meaningful way. Validated with three geometries—a thin-walled structure, a cylindrical part, and a cubic part—the highlights of this work are summarized as follows.

- Integrating residuals of transient heat transfer equations, boundary condition, and initial condition as a physics-based regularization penalty improves model accuracy compared to the loss solely based on data.
- Instead of inputting raw process parameters directly into the model, a Physics-informed input—laser heat flux in this paper—is utilized to better capture the relationship between process parameters and the temperature field. This Physics-informed input demonstrates a positive impact on the model's accuracy.
- The proposed framework achieves high accuracy, with an error below 3 % for full field temperature prediction in a thin-walled part and below 1 % for 2D temperature fields in cylindrical and cubic parts for subsequent timestamps. These results suggest the framework's potential adaptability to different scenarios involving varying process parameters, geometries, and deposition patterns, without requiring changes to the core model. The proposed framework excels in predicting temperature fields for extended future periods, employing both rolling and direct prediction approaches. The direct approach demonstrates superior potential for longer-term predictions, while the rolling approach provides insights into thermal dynamics at a lower computational cost.

It is important to note that the current work focuses on real-time prediction, while real-time learning could be explored as a future extension. Future work will focus on advancing the current framework to enable online training, allowing for the continual updating of model parameters using real-time data acquired during the manufacturing process.

CRediT authorship contribution statement

Pouyan Sajadi: Writing – review & editing, Writing – original draft, Visualization, Methodology, Investigation, Conceptualization. **Mostafa Rahmani Dehaghani:** Writing – review & editing, Conceptualization. **Yifan Tang:** Writing – review & editing, Conceptualization. **G. Gary Wang:** Writing – review & editing, Supervision, Funding acquisition, Conceptualization.

Declaration of Generative AI and AI-assisted technologies in the writing process

In the process of preparing this work, the authors utilized ChatGPT to make subtle refinements, contributing to the overall polish of the text. After incorporating this tool, the authors conducted a careful review and made necessary edits to ensure the publication's quality, taking full responsibility for the final content.

Declaration of competing interest

The authors declare the following financial interests/personal

relationships which may be considered as potential competing interests: Pouyan Sajadi, Yifan Tang reports financial support was provided by Natural Sciences and Engineering Research Council of Canada. If there are other authors, they declare that they have no known competing financial interests or personal relationships that could have appeared to influence the work reported in this paper.

Acknowledgements

Funding from the Natural Sciences and Engineering Research Council (NSERC) of Canada under the project RGPIN-2019-06601.

Data availability

Data will be made available on request.

References

Bai, X., Zhang, H., Wang, G., 2013. Improving prediction accuracy of thermal analysis for weld-based additive manufacturing by calibrating input parameters using IR imaging. Int. J. Adv. Des. Manuf. Technol. 69, 1087–1095.

Barua, S., Liou, F., Newkirk, J., Sparks, T., 2014. Vision-based defect detection in laser metal deposition process. Rapid Prototyp. J. 20, 77–85.

Bernauer, C., Zapata, A., Zaeh, M.F., 2022. Toward defect-free components in laser metal deposition with coaxial wire feeding through closed-loop control of the melt pool temperature. J. Laser Appl. 34.

Bontha, S., Klingbeil, N.W., Kobryn, P.A., Fraser, H.L., 2006. Thermal process maps for predicting solidification microstructure in laser fabrication of thin-wall structures. J. Mater. Process. Technol. 178, 135–142. https://doi.org/10.1016/j.jmatprotec.2006.03.155.

Busachi, A., Erkoyuncu, J., Colegrove, P., Martina, F., Watts, C., Drake, R., 2017. A review of Additive Manufacturing technology and Cost Estimation techniques for the defence sector. CIRP J Manuf Sci Technol 19, 117–128.

Byrd, R.H., Lu, P., Nocedal, J., Zhu, C., 1995. A limited memory algorithm for bound constrained optimization. SIAM J. Sci. Comput. 16, 1190–1208.

Chaurasia, P.K., Goecke, S.F., De, A., 2023. Towards real-time monitoring of metal transfer and melt pool temperature field in gas metal arc directed energy deposition. Weld. World 67, 1781–1791.

Darabi, R., Ferreira, A., Azinpour, E., de Sa, J.C., Reis, A., 2022. Thermal study of a cladding layer of Inconel 625 in Directed Energy Deposition (DED) process using a phase-field model. Int. J. Adv. Des. Manuf. Technol. 119, 3975–3993.

Denlinger, E.R., Michaleris, P., 2016. Effect of stress relaxation on distortion in additive manufacturing process modeling. Addit. Manuf. 12, 51–59.

Heigel, J.C., Michaleris, P., Reutzel, E.W., 2015. Thermo-mechanical model development and validation of directed energy deposition additive manufacturing of Ti–6Al–4V. Addit. Manuf. 5, 9–19.

Holman, J.P., 1986. Heat Transfer. McGraw Hill.

Hosseini, E., Gh Ghanbari, P., Müller, O., Molinaro, R., Mishra, S., 2023. Single-track thermal analysis of laser powder bed fusion process: parametric solution through physics-informed neural networks. Comput. Methods Appl. Mech. Eng. 410. https://doi.org/10.1016/j.cma.2023.116019.

Jiang, F., Xia, M., Hu, Y., 2023. Physics-informed machine learning for accurate prediction of temperature and melt pool dimension in metal additive manufacturing. 3D Print. Addit. Manuf. https://doi.org/10.1089/3dp.2022.0363.

Jin, X., Cai, S., Li, H., Karniadakis, G.E., 2021. NSFnets (Navier-Stokes flow nets): physics-informed neural networks for the incompressible Navier-Stokes equations. J. Comput. Phys. 426, 109951. https://doi.org/10.1016/j.jcp.2020.109951.

Karmiris-Obratański, P., Papazoglou, E.L., Karkalos, N.E., Hontzopoulos, E., Markopoulos, A.P., 2022. On the laser beam absorption efficiency in laser welding of aluminium thin sheet with copper pipe. In: IOP Conference Series: Materials Science and Engineering. IOP Publishing, 012017.

Khairallah, S.A., Anderson, A.T., Rubenchik, A., King, W.E., 2016. Laser powder-bed fusion additive manufacturing: physics of complex melt flow and formation mechanisms of pores, spatter, and denudation zones. Acta Mater. 108, 36–45. https://doi.org/10.1016/j.actamat.2016.02.014.

Kingma, D.P., Ba, J., 2014. Adam: a method for stochastic optimization. arXiv preprint arXiv:1412.6980.

Li, S., Wang, G., Di, Y., Wang, L., Wang, H., Zhou, Q., 2023. A physics-informed neural network framework to predict 3D temperature field without labeled data in process of laser metal deposition. Eng. Appl. Artif. Intell. 120, 105908. https://doi.org/10.1016/j.engappai.2023.105908.

Li, X., Zhao, C., Sun, T., Tan, W., 2020. Revealing transient powder-gas interaction in laser powder bed fusion process through multi-physics modeling and high-speed synchrotron x-ray imaging. Addit. Manuf. 35, 101362.

Liao, S., Webster, S., Huang, D., Council, R., Ehmann, K., Cao, J., 2022a. Simulation-guided variable laser power design for melt pool depth control in directed energy deposition. Addit. Manuf. 56, 102912.

Liao, S., Xue, T., Jeong, J., Webster, S., Ehmann, K., Cao, J., 2022b. Hybrid thermal modeling of additive manufacturing processes using physics-informed neural networks for temperature prediction and parameter identification. https://doi.org/10.1007/s00466-022-02257-9.

Lippold, J.C., Kiser, S.D., DuPont, J.N., 2011. Welding Metallurgy and Weldability of Nickel-Base Alloys. John Wiley & Sons.

Marshall, G.J., Thompson, S.M., Shamsaei, N., 2016a. Data indicating temperature response of Ti–6Al–4V thin-walled structure during its additive manufacture via Laser Engineered Net Shaping. Data Brief 7, 697–703.

Marshall, G.J., Young, W.J., Thompson, S.M., Shamsaei, N., Daniewicz, S.R., Shao, S., 2016b. Understanding the microstructure formation of Ti-6Al-4V during direct laser deposition via in-situ thermal monitoring. Jom 68, 778–790.

Mozaffar, M., Paul, A., Al-Bahrani, R., Wolff, S., Choudhary, A., Agrawal, A., Ehmann, K., Cao, J., 2018. Data-driven prediction of the high-dimensional thermal history in directed energy deposition processes via recurrent neural networks. Manuf Lett 18, 35–39.

Neupane, D., Kim, Y., Seok, J., Hong, J., 2021. CNN-based fault detection for smart manufacturing. Appl. Sci. 11, 11732.

Ning, F., Jiang, D., Liu, Z., Wang, H., Cong, W., 2021. Ultrasonic frequency effects on the melt pool formation, porosity, and thermal-dependent property of Inconel 718 fabricated by ultrasonic vibration-assisted directed energy deposition. J. Manuf. Sci. Eng. 143, 051009.

Noakoasteen, O., Wang, S., Peng, Z., Christodoulou, C., 2020. Physics-informed deep neural networks for transient electromagnetic analysis. IEEE Open Journal of Antennas and Propagation 1, 404–412.

Paul, A., Mozaffar, M., Yang, Z., Liao, W., Choudhary, A., Cao, J., Agrawal, A., 2019. A real-time iterative machine learning approach for temperature profile prediction in additive manufacturing processes. In: 2019 IEEE International Conference on Data Science and Advanced Analytics (DSAA). IEEE, pp. 541–550.

Raissi, M., Perdikaris, P., Karniadakis, G.E., 2019. Physics-informed neural networks: a deep learning framework for solving forward and inverse problems involving nonlinear partial differential equations. J. Comput. Phys. 378, 686–707.

Razavykia, A., Brusa, E., Delprete, C., Yavari, R., 2020. An overview of additive manufacturing technologies—a review to technical synthesis in numerical study of selective laser melting. Materials 13, 3895.

Ren, K., Chew, Y., Fuh, J.Y.H., Zhang, Y.F., Bi, G.J., 2019. Thermo-mechanical analyses for optimized path planning in laser aided additive manufacturing processes. Mater. Des. 162, 80–93. https://doi.org/10.1016/j.matdes.2018.11.014.

Ren, K., Chew, Y., Zhang, Y.F., Fuh, J.Y.H., Bi, G.J., 2020a. Thermal field prediction for laser scanning paths in laser aided additive manufacturing by physics-based machine learning. Comput. Methods Appl. Mech. Eng. 362, 112734.

Ren, X., Chai, Z., Xu, J., Zhang, X., He, Y., Chen, H., Chen, X., 2020b. A new method to achieve dynamic heat input monitoring in robotic belt grinding of Inconel 718. J. Manuf. Process. 57, 575–588.

Roberts, I.A., Wang, C.J., Esterlein, R., Stanford, M., Mynors, D.J., 2009. A three-dimensional finite element analysis of the temperature field during laser melting of metal powders in additive layer manufacturing. Int. J. Mach. Tool Manufact. 49, 916–923.

Roy, M., Wodo, O., 2020. Data-driven modeling of thermal history in additive manufacturing. Addit. Manuf. 32, 101017.

Saldi, Z., Pasang, T., Khogres, W., Budiman, A., Gunawan, F., 2024. Numerical simulations of fluid flows and heat transfer in melt pools of Directed Energy Deposition of SS316L. In: E3S Web of Conferences. EDP Sciences, 03010.

Shamsaei, N., Yadollahi, A., Bian, L., Thompson, S.M., 2015. An overview of Direct Laser Deposition for additive manufacturing; Part II: mechanical behavior, process parameter optimization and control. Addit. Manuf. 8, 12–35. https://doi.org/10.1016/j.addma.2015.07.002.

Sherstinsky, A., 2020. Fundamentals of recurrent neural network (RNN) and long short-term memory (LSTM) network. Physica D 404, 132306.

Shi, X., Chen, Z., Wang, H., Yeung, D.-Y., Wong, W.-K., Woo, W., 2015. Convolutional LSTM network: a machine learning approach for precipitation nowcasting. Adv. Neural Inf. Process. Syst. 28.

Shukla, K., Di Leoni, P.C., Blackshire, J., Sparkman, D., Karniadakis, G.E., 2020. Physics-informed neural network for ultrasound nondestructive quantification of surface breaking cracks. J. Nondestruct. Eval. 39, 1–20.

Siahvashi, N., Hamdami, M., Arabanian, A.S., Massudi, R., 2021. Increasing the power and quality of beam in coherent combination of laser beams by controlling optical axis angles. Opt. Quant. Electron. 53, 1–15.

Stathatos, E., Vosniakos, G.-C., 2019. Real-time simulation for long paths in laser-based additive manufacturing: a machine learning approach. Int. J. Adv. Des. Manuf. Technol. 104, 1967–1984.

Tang, Y., Dehaghani, M.R., Sajadi, P., Balani, S.B., Dhalpe, A., Panicker, S., Wu, D., Coatanea, E., Wang, G.G., 2023. Online thermal field prediction for metal additive manufacturing of thin walls. J. Manuf. Process. 108, 529–550.

Thompson, S.M., Bian, L., Shamsaei, N., Yadollahi, A., 2015. An overview of Direct Laser Deposition for additive manufacturing; Part I: transport phenomena, modeling and diagnostics. Addit. Manuf. 8, 36–62. https://doi.org/10.1016/j.addma.2015.07.001.

Wu, T.-W., Zhang, H., Peng, W., Lü, F., He, P.-J., 2023. Applications of convolutional neural networks for intelligent waste identification and recycling: a review. Resour. Conserv. Recycl. 190, 106813.

Xie, J., Chai, Z., Xu, L., Ren, X., Liu, S., Chen, X., 2022a. 3D temperature field prediction in direct energy deposition of metals using physics informed neural network. Int. J. Adv. Manuf. Technol. 119, 3449–3468. https://doi.org/10.1007/s00170-021-08542-w.

Xie, J., Chai, Z., Xu, L., Ren, X., Liu, S., Chen, X., 2022b. 3D temperature field prediction in direct energy deposition of metals using physics informed neural network. Int. J. Adv. Des. Manuf. Technol. 119, 3449–3468.

Yan, H., Shen, L., Wang, X., Tian, Z., Xu, G., Xie, D., Liang, H., 2018a. Stress and deformation evaluation of the subarea scanning effect in direct laser-deposited Ti-6Al-4V. Int. J. Adv. Des. Manuf. Technol. 97, 915–926.

Yan, J., Yan, W., Lin, S., Wagner, G.J., 2018b. A fully coupled finite element formulation for liquid–solid–gas thermo-fluid flow with melting and solidification. Comput. Methods Appl. Mech. Eng. 336, 444–470.

Yan, Z., Liu, W., Tang, Z., Liu, X., Zhang, N., Li, M., Zhang, H., 2018c. Review on thermal analysis in laser-based additive manufacturing. Opt Laser. Technol. 106, 427–441. https://doi.org/10.1016/j.optlastec.2018.04.034.

Yao, J.-F., Yang, Y., Wang, X.-C., Zhang, X.-P., 2023. Systematic review of digital twin technology and applications. Vis Comput Ind Biomed Art 6, 10.

Yu, Y., Si, X., Hu, C., Zhang, J., 2019. A review of recurrent neural networks: LSTM cells and network architectures. Neural Comput. 31, 1235–1270.

Zhang, L., Chen, X., Zhou, W., Cheng, T., Chen, L., Guo, Z., Han, B., Lu, L., 2020. Digital twins for additive manufacturing: a state-of-the-art review. Appl. Sci. 10, 8350.

Zheng, B., Zhou, Y., Smugeresky, J.E., Schoenung, J.M., Lavernia, E.J., 2008. Thermal behavior and microstructural evolution during laser deposition with laser-engineered Net shaping: Part I. Numerical calculations. Metall. Mater. Trans. 39, 2228–2236. https://doi.org/10.1007/s11661-008-9557-7.

Zhou, S.K., Greenspan, H., Davatzikos, C., Duncan, J.S., Van Ginneken, B., Madabhushi, A., Prince, J.L., Rueckert, D., Summers, R.M., 2021. A review of deep learning in medical imaging: imaging traits, technology trends, case studies with progress highlights, and future promises. Proc. IEEE 109, 820–838.

Zhu, Q., Liu, Z., Yan, J., 2021. Machine learning for metal additive manufacturing: predicting temperature and melt pool fluid dynamics using physics-informed neural networks. Comput. Mech. 67, 619–635. https://doi.org/10.1007/s00466-020-01952-9.